Applied Energy 215 (2018) 75–86

Contents lists available at ScienceDirect

Applied Energy

journal homepage: www.elsevier.com/locate/apenergy

The membrane-assisted chemical looping reforming concept for efficient H_2 production with inherent CO_2 capture: Experimental demonstration and model validation

J.A. Medrano[a], I. Potdar[a], J. Melendez[b], V. Spallina[a,b], D.A. Pacheco-Tanaka[b], M. van Sint Annaland[a], F. Gallucci[a,*]

[a] Chemical Process Intensification, Department of Chemical Engineering and Chemistry, Eindhoven University of Technology, De Rondom, 70 5612 AP Eindhoven, The Netherlands
[b] TECNALIA, Energy and Environment/Industry and Transport Divisions, Mikeletegi Pasealekua 2, 20009 San Sebastián-Donostia, Spain

HIGHLIGHTS

- A new reactor concept has been experimentally demonstrated at lab-scale.
- A phenomenological model has been developed and validated with experimental data.
- Methane conversions above 90% at intermediate temperatures.
- Hydrogen recoveries above 30% at low pressure operation.

GRAPHICAL ABSTRACT

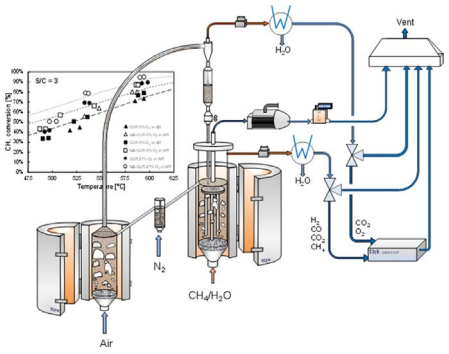

ARTICLE INFO

Keywords:
Membrane reactor
H_2 production
Chemical Looping
Steam methane reforming

ABSTRACT

In this work a novel reactor concept referred to as Membrane-Assisted Chemical Looping Reforming (MA-CLR) has been demonstrated at lab scale under different operating conditions for a total working time of about 100 h. This reactor combines the advantages of Chemical Looping, such as CO_2 capture and good thermal integration, with membrane technology for a better process integration and direct product separation in a single unit, which in its turn leads to increased efficiencies and important benefits compared to conventional technologies for H_2 production. The effect of different operating conditions (i.e. temperature, steam-to-carbon ratio or oxygen feed in the reactor) has been evaluated in a continuous chemical looping reactor, and methane conversions above 90% have been measured with (ultra-pure) hydrogen recovery from the membranes. For all the cases a maximum recovery factor of around 30% has been measured, which could be increased by operating the concept at higher pressures and with more membranes. The optimum conditions have been found at temperatures around 600 °C for a steam-to-carbon ratio of 3 and diluted air in the air reactor (5% O_2). The complete demonstration has been carried out feeding up to 1 L/min of CH_4 (corresponding to 0.6 kW of thermal input) while up to 1.15 L/min of H_2 was recovered.

Simultaneously, a phenomenological model has been developed and validated with the experimental results. In general, good agreement is observed, with overall deviations below 10% in terms of methane conversion, H_2 recovery and separation factor. The model allows better understanding of the behavior of the MA-CLR concept and the optimization and design of scaled-up versions of the concept.

* Corresponding author.
E-mail address: f.gallucci@tue.nl (F. Gallucci).

https://doi.org/10.1016/j.apenergy.2018.01.087
Received 24 August 2017; Received in revised form 12 January 2018; Accepted 28 January 2018
Available online 20 February 2018
0306-2619/ © 2018 The Author(s). Published by Elsevier Ltd. This is an open access article under the CC BY license (http://creativecommons.org/licenses/BY/4.0/).

Nomenclature

Acronyms and abbreviations

CCS	carbon capture and storage
CLC	chemical looping combustion
CLR	chemical looping reforming
HRF	hydrogen recovery factor
MA-CLR	membrane assisted chemical looping reforming
SMR	steam methane reforming
SF	separation factor
PSA	pressure swing adsorption
O/C	oxygen to carbon ratio
S/C	steam to carbon ratio
WGS	water gas shift

Symbols and units

Ar	Archimedes number
b	gas solid reaction stoichiometric factor [mol_s/mol_g]
C_i	gas concentration of component i [mol/m^3]
C_s	solid concentration [mol/m^3]
d_b	bubble diameter [m]
$d_{b,max}$	maximum bubble diameter [m]
D_0	gas diffusion coefficient [m^2/s]
d_p	particle diameter [m]
E_0	activation energy [kJ/mol]
E_D	activation energy for gas-solid reactions [kJ/mol]
f_b	bubble fraction –
f_c	cloud fraction –
f_{ce}	cloud-emulsion fraction –
f_w	wake fraction –
g	gravitational constant [m/s^2]
k_0	pre-exponential factor
k_{bc}	gas exchange coefficient between the bubble and cloud phases [s^{-1}]
k_{be}	gas exchange coefficient between the bubble and emulsion phases [s^{-1}]
k_{ce}	gas exchange coefficient between the cloud and emulsion phases [s^{-1}]
K_p	equilibrium constant
k_x	solid diffusion decay constant –
n	exponential factor –
P	pressure [bar]
$r_{SMR/WGS}$	reaction rates for the gas phase [mol/m^3 s]
r_0	PARTICLE grain radius at reference point [m]
Re	Reynolds number –
u_0	superficial gas velocity [m/s]
u_b	bubble velocity [m/s]
$u_{g,e}$	gas velocity in the emulsion phase [m/s]
u_{mf}	minimum fluidization velocity [m/s]
T	temperature [°C]
x	molar fraction [mol_i/mol_g]

Greek letters

α	wake parameter –
β	mass transfer resistance coefficient –
δ	bubble fraction in the bed –
$\Delta H^\circ_{298\ K}$	enthalpy of reaction at 298 K [kJ/mol]
ε_{mf}	bed voidage at incipient fluidization conditions –
ε_s	bed porosity –
μ_g	dynamic viscosity of the gas [Pa s]
ρ_g	bulk catalyst density [kg/m^3]
ρ_g	gas density [kg/m^3]
ρ_s	particle density [kg/m^3]

Subscripts

0	reference point
b	bubble
cat	catalyst
ce	cloud-emulsion
Equil	equilibrium
g	gas
in	inlet
mf	minimum fluidization
out	outlet
perm	permeate
s	solid
ret	retentate
w	wake

1. Introduction

The concentration of greenhouse gases has increased since the pre-industrial period, driven largely by economic and population growth. This has led to atmospheric concentrations of carbon dioxide, methane and nitrous oxide unprecedented in at least the last 800,000 years [1]. The main greenhouse gases are H_2O, CO_2, CH_4, N_2O, CFC's and SF_6, and their potential can be classified depending on the volume of emissions and persistency in the atmosphere. According to these two parameters, CO_2 has the largest contribution to the greenhouse effect by far. Nowadays, the global atmospheric CO_2 concentration exceeds 400 ppm, very far from pre-industrial values (280 ppm) and an increase to 426–936 ppm is projected for the 21st century depending on different scenarios [1]. Only emission scenarios limiting CO_2 concentrations to about 450 ppm in 2100 are likely to maintain global warming below 2 °C by the end of this century.

The Intergovernmental Panel on Climate Change [2], in collaboration with the International Energy Agency [3], reviewed different technological strategies to reduce the net CO_2 emissions. The long term solution is the total replacement of current fossil fuels by renewable energy sources. However, a midterm strategy is required, mainly considering that fossil fuels are still the most important sources worldwide for energy conversion processes. A feasible midterm solution to mitigate CO_2 emissions to the atmosphere coming from fossil fuels is referred to as Carbon Capture and Storage (CCS), which could account up to 19% of the total reduction in emissions needed. In CCS a relatively pure stream of carbon dioxide from industrial and energy-related sources is sequestrated, i.e. conditioned, compressed and sent for long term storage.

Capture of CO_2 from fossil fuels and/or biomass can be carried out at different stages in industrial power and heat production processes: post-combustion capture, pre-combustion capture and oxyfuel strategy [2,4]. However, implementation of CCS systems with state-of-the-art industrial technologies requires costly gas separation units with high energy costs that limit the overall efficiency of the process, as already demonstrated in different publications in the literature. For instance, the equivalent global efficiency of H_2 production via the benchmark steam reforming technology of methane/natural gas might drop from 80% to 67%, when a current pre-combustion technology is implemented, as reported by Spallina et al. [5]. In the case of coal

gasification for hydrogen production, CO_2 transport and storage would increase hydrogen production costs by about 10–15% [6]. These studies show that the efficiency penalty is the main limiting factor for the implementation of CCS systems in benchmark technologies and still many efforts are required to improve these separation steps.

As reviewed by the IPCC in 2005 [2], a promising technology for oxyfuel CCS capture is Chemical Looping [7–10], which has been successfully investigated for power generation (Chemical Looping Combustion, CLC) and for fuel partial oxidation (Chemical Looping Reforming or Gasification, CLR). The idea behind Chemical Looping is to divide the conversion of the fuel into separated oxidation and reduction stages by means of a solid material transferring oxygen. In this technology, the separation of oxygen from air is accomplished by fixing the oxygen to a metal (oxide), as schematically presented in Fig. 1. This (often supported) metal/metal oxide particle is referred to as oxygen carrier. While in the so-called air reactor the oxygen carrier is oxidized (regenerated), it releases the oxygen needed in the fuel reactor, which operates at reducing atmospheres in the presence of the fuel. Often, an interconnected fluidized bed reactor system has been proposed, as reviewed by Adanez et al. [11], where the solids circulation rate between the two reactors strongly determines the energy balance in both reactors, and thus the performance of this technology. The main advantage of chemical looping compared to conventional technologies is the absence of N_2 in the fuel reactor. This implies a high-purity stream of carbon dioxide in chemical looping combustion for power generation, or lower O_2 consumptions in chemical looping reforming (CLR) [12]. In chemical looping reforming, the fuel conversion produces a reformed syngas with a high H_2 concentration and the technology works as an autothermal reformer, where the heat for the endothermic reactions is supplied by partial oxidation of the fuel gas in the fuel reactor. Further information on Chemical Looping can be found in the open literature [11,13–19].

Another strategy to limit the CO_2 concentration in the atmosphere to below 450 ppm in 2100 is the substitution of fossil fuels by clean energy carriers like H_2, which does not produce CO_2 in its final use [20,21]. However, H_2 does not exist as a gas on earth, but has to be first produced. The benchmark technology for H_2 production is the conversion of natural gas in fixed bed tubular reformers at high temperature and high pressure, referring to as Steam Methane Reforming (SMR). However, this process is one of the main contributors to CO_2 emissions to the atmosphere. At this stage, the combined use of fossil fuels and the necessity of high-purity H_2 production drives the current research towards an increase in the efficiency of the Steam Methane Reforming process with CO_2 capture.

A novel technology in the framework of process intensification is the use of membrane reactors [22–26]. In a membrane reactor, chemical reaction and product separation occur in the same unit, thus achieving an important process integration which accomplishes a reduction in the required number of process units even when aiming for CO_2 capture. In equilibrium limited reaction systems, the selective separation of a product of the reaction (i.e. H_2), implies the displacement of the thermodynamic equilibria towards products following *Le Chatelier's* principle. This accomplishes an enhancement in the fuel conversion, while the separation of a pure product from the membrane is occurring at the same time. In H_2 production processes, supported Pd-based membranes show the best compromise between the permeation rate through the membrane, the perm-selectivity, mechanical and chemical stability and costs among other options and represent the preferred material compared to other noble metals [22]. However, the heat management when integrating CO_2 capture is not straightforward in a membrane reactor, mostly because the system is overall highly endothermic and heat should be supplied externally unless challenging configurations are adopted [27,28].

The combination of Chemical Looping and membrane reactors has the potential of merging in an efficient way direct CO_2 capture and (ultra) pure H_2 production. This novel reactor concept was thermodynamically proposed by Medrano et al. [29] under the name *Membrane-Assisted Chemical Looping Reforming (MA-CLR)*. In this system, a fluidized bed membrane reactor substitutes the fuel reactor of the Chemical Looping concept, whereas the oxygen carrier has a double functionality. On the one hand the solid metal transfers the oxygen needed for the partial oxidation of the fuel in the membrane reactor and is used for a proper heat balance. On the other hand, when the oxygen carrier is reduced in the membrane reactor, it behaves as a catalyst for fuel reforming. A representation of the MA-CLR concept is given in Fig. 2. In this concept, both catalytic and gas-solid reactions are occurring simultaneously. The different reactions (using a Ni-based oxygen carrier) are reported in reactions R1-R6.

Catalytic reactions

Steam Methane Reforming $CH_4 + H_2O \leftrightarrow CO + 3H_2 \quad \Delta H°_{298K} = +206\ kJ/mol$ (R1)

Water Gas Shift $CO + H_2O \leftrightarrow CO_2 + H_2 \quad \Delta H°_{298K} = -41.1\ kJ/mol$ (R2)

Gas-solid reactions

Oxidation of Ni $2Ni + O_2 \rightarrow 2NiO \quad \Delta H°_{298K} = -488\ kJ/mol$ (R3)

Reduction of NiO with CH_4 $NiO + CH_4 \rightarrow Ni + CO + 2H_2 \quad \Delta H°_{298K} = +204\ kJ/mol$ (R4)

Reduction of NiO with H_2 $NiO + H_2 \rightarrow Ni + H_2O \quad \Delta H°_{298K} = +2.48\ kJ/mol$ (R5)

Reduction of NiO with CO $NiO + CO \rightarrow Ni + CO_2 \quad \Delta H°_{298K} = -38.6\ kJ/mol$ (R6)

Thermodynamic analysis confirmed the potential of this concept compared with other concepts proposed in the literature [24]. Also a detailed techno-economic analysis of this concept was carried out and compared with the benchmark steam reforming technology for H_2 production [5]. From the results of the techno-economic analysis, it has been found that the use of Pd-based membranes do not compromise the H_2 production costs since their net capital costs are similar to PSA and CO_2 separation units. Compared to traditional technologies, the MA-CLR shows higher equivalent reforming efficiencies and lower H_2 production costs (0.19 €/Nm^3H_2 for MA-CLR and 0.21 and 0.28 €/Nm^3H_2 for the benchmark technology without and with CO_2 capture). Therefore, the potential found for the MA-CLR concept through these previous investigations needs to be demonstrated experimentally.

In this work, the MA-CLR has been for the first time operated and demonstrated in a continuous chemical looping system at lab scale level. In this concept, three perm-selective metallic supported Pd-based membranes have been immersed in the fuel reactor, and a commercial Ni-based catalyst provided by Johnson Matthey has been selected as oxygen carrier and catalyst for the concept [30].

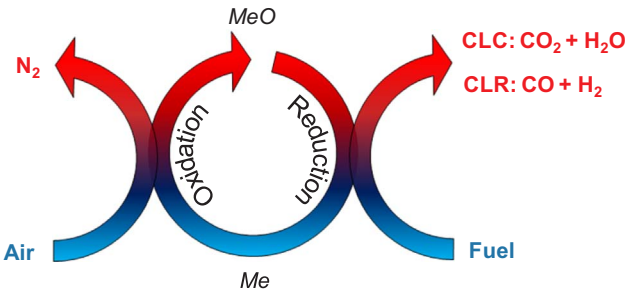

Fig. 1. Schematic representation of the Chemical Looping process.

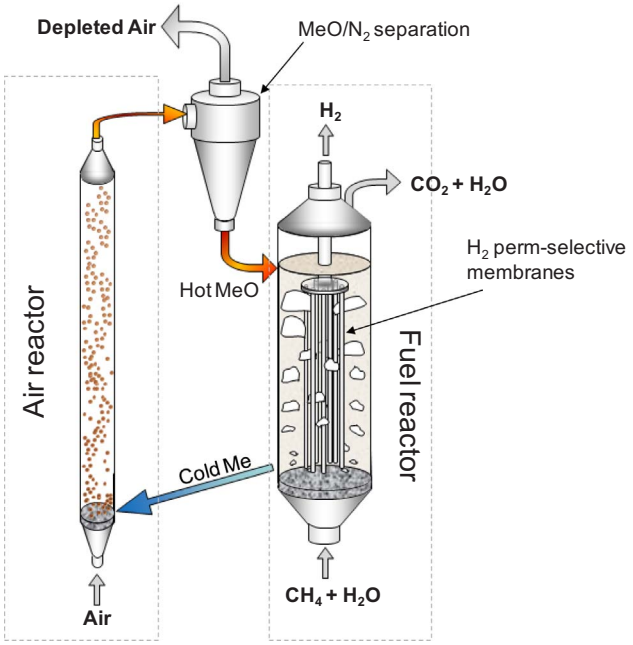

Fig. 2. Schematic representation of the MA-CLR concept for pure H_2 production via Pd-based selective membranes combined with CO_2 capture via chemical looping.

Simultaneously, in order to better understand the behavior of the MA-CLR concept, a 1D phenomenological model has been developed and validated in this work. This model is based on the approach described in the work of Iliuta et al. [31], who adjusted the bubbling bed model from Kunii and Levenspiel [32] for a chemical looping system. The objective behind the model is that it should be reliable and validated with experimental data, so that results can be extrapolated to larger scales, which in its turn can help in designing larger reactors in future works.

In the following sections, first the phenomenological model is presented. Afterward, a detailed description of the lab-scale reactor is given together with the selected experimental conditions tested for the demonstration of the MA-CLR concept. Subsequently, the experimental demonstration is presented and the experimental results are compared with calculation results obtained with the developed phenomenological model and they are thoroughly discussed. Finally, several guidelines and recommendations for further development are given together with the general conclusions obtained from this work.

2. Phenomenological model

The model is based on the approach presented by Iliuta et al. [31], who adopted the 1D continuum model describing the three phase system of the bubbling bed model from Kunii and Levenspiel [32] and modified it for a chemical looping interconnected fluidized bed system. A scheme of the system is presented in Fig. 3. In this model, both the gas and the solid phases are described. The gas phase is fed into the reactors at a superficial gas velocity (u_0) above the minimum fluidization velocity (u_{mf}) and forms a bubble phase with fraction f_b with a characteristic bubble diameter (d_b) as a function of the axial position. The remaining gas moves upwards in the emulsion phase at the emulsion velocity (u_e) and the gas is exchanged with the gas in the bubble phase (K_{be}). A bubble solids hold-up of 0.025 is selected as suggested in literature [33]. The wake with a fraction α relative to the bubble fraction moves upwards with a velocity equal to the bubble velocity (u_b) and has the porosity of the emulsion phase, which is assumed at minimum fluidization conditions (ε_{mf}). On the other hand, solids move downwards in the emulsion phase at a velocity $u_{e,s}$ and are exchanged with the solids in the wake-bubble phase ($K_{we,s}$).

The model is simplified to steady state conditions and a general mass balance can be written for the gas phase in the bubble and emulsion phases as stated in Eqs. (1) and (2), respectively. A summary of the hydrodynamics (Eqs. (3)–(10)) and mass transfer (Eq. (11)) correlations used in this work is reported in Table 1. The current version of the model does not solve the energy balance of the system and the temperature along each reactor is considered to be constant.

Bubble phase:

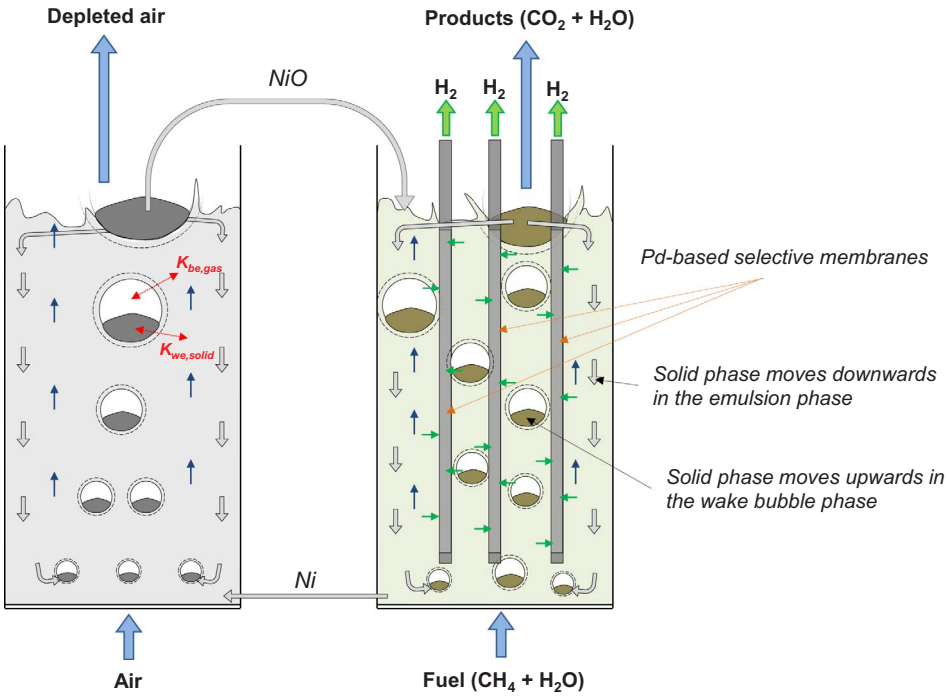

Fig. 3. Schematic representation of the phenomenological model developed in this work to investigate the behavior of the MA-CLR concept.

Table 1
Summary of the correlations used for hydrodynamics and mass transfer.

Hydrodynamics			
Minimum fluidization velocity	$\frac{Ar}{Re_{mf}} = 150\frac{1-\varepsilon_{mf}}{\phi^2\varepsilon_{mf}^3} + 1.75\frac{Re_{mf}}{\phi\varepsilon_{mf}^3}$ $with\ Ar = \frac{d_p^3\rho_g(\rho_p-\rho_g)g}{\mu_g^2}$ $and\ Re_{mf} = \frac{\rho_g u_{mf} d_p}{\mu_g}$	[34]	(3)
Minimum fluidization voidage	$\varepsilon_{mf} = 0.586Ar^{-0.029}(\frac{\rho_g}{\rho_p})^{0.021}$	[35]	(4)
Bubble diameter	$d_b = d_{b,max} - (d_{b,max} - d_{b,0})e^{-\frac{0.3h}{D_T}}$ $d_{b,max} = 0.65(\frac{\pi}{4}D_T^2(u_0-u_{mf}))$ $d_{b,0} = 0.376(u_0-u_{mf})^2$	[36] [32] [32]	(5)
Bubble velocity	$u_b = u_0 - u_{mf} + 0.711(gd_b)^{0.5}$	[32]	(6)
Emulsion velocity	$u_{g,e} = \frac{u_0 - (f_b + f_w\varepsilon_{mf})u_b}{f_{ce}\varepsilon_{mf}}$		(7)
Bubble fraction	$f_b \approx \frac{u_0 - u_{mf}}{u_b}$	[32]	(8)
Wake fraction	$f_w = \alpha f_b\ with\ \alpha = 1 - e^{-4.92d_b}$	[33]	(9)
Emulsion fraction	$f_{ce} = 1 - (f_b + f_w)$		(10)
Mass transfer			
Mass transfer coefficients gas phase	$K_{i,be} = \frac{4}{d_b}(\frac{2.6u_0}{\pi})$	[37]	(11)

$$\frac{\partial}{\partial z}[u_b(f_b + f_w\varepsilon_{mf})C_{i,bw}] = K_{i,be}(f_b + f_w\varepsilon_{mf})(C_{i,ce} - C_{i,bw}) \pm R_{i,bw}f_{bw}(1-\varepsilon_{mf}) \quad (1)$$

Emulsion phase:

$$\frac{\partial}{\partial z}[u_{g,e}(f_{ce}\varepsilon_{mf})C_{i,ce}] = -K_{i,be}(f_b + f_w\varepsilon_{mf})(C_{i,ce} - C_{i,bw}) \pm R_{i,ce}f_{ce}(1-\varepsilon_{mf}) \quad (2)$$

The molar expansion as consequence of the reforming reaction is accounted for in the model by solving the total mass balance for every axial position. This is done by evaluating the emulsion gas velocity as presented in Eq. (7) in Table 1. Similarly, as for the gas phase, the solid phase is solved at each axial position in the bed and a general mass balance can be written for the wake phase moving upwards in the bed and the emulsion phase moving in downwards (Eqs. (12) and (13)). In this case, the solids velocity in the emulsion phase (downwards) is calculated from the mass balance in each position (Eq. (14)) as shown in Table 2. Finally, the solids mixing between the wake and emulsion phases is calculated from the correlation described in the work of Gascon et al. [38] and presented in Eq. (15).

The solid phase used in the model (also for the experimental demonstration) is the commercial Ni-based oxygen carrier investigated in the literature for low temperature chemical looping applications, from where the gas-solid reaction rate expressions are used [30]. From the gas-solid reaction rate expressions, and also according to experimental observations, it is evidenced that CH_4 does not reduce NiO at the considered operating conditions. Therefore, a small fraction of reduced Ni is required in order to promote the reforming reaction, so that H_2 and CO reduce the NiO oxygen carrier. The catalytic kinetic expressions are obtained from the work of Numaguchi and Kikuchi [39]. An overview on the kinetics expressions for the heterogeneous catalyzed gas phase reactions (Eqs. (16) and (17)) and gas-solid reactions (Eqs. (18)–(21)) is provided in Table 3 and Table 4 respectively.

The gas phase represents an initial boundary problem where the input should be specified. On the other hand, the solids phase represents a boundary value problem. It refers to the solids circulation rates from one reactor to the other one and vice versa. It is assumed that oxidized oxygen carrier moving upwards in the wake phase on the top of the air reactor is split into two different streams. One is entering at the top of the fuel reactor in the emulsion phase, while the other part is incorporated into the emulsion phase in the air reactor. Similarly, solids at the bottom of the fuel reactor are split into solids entering into the wake phase of the bubbles in the fuel reactor and solids circulated to the bottom of the air reactor in the wake phase. This solid circulation is also schematically represented in Fig. 3. Therefore, to accurately solve the general mass balance, gas and solid hydrodynamics should be solved at once to satisfy the boundary conditions.

The placement of membranes inside the fuel reactor is simulated by imposing as condition that the maximum bubble diameter is equal to the minimum distance between two membranes. Gas permeation through the membranes follows a Fick's law expression (Eqs. (22) and (23)) and the main parameters are the ones summarized in the work of Fernandez et al. [40] for a Pd-based metallic supported membrane (as also used in this work) and are depicted in Table 5. For the model, it is assumed that ideally only H_2 can permeate through the membranes (i.e. infinite perm-selectivity). As it is difficult to predict from which phase the H_2 is permeating, it is assumed that the total amount of H_2 permeated comes from both emulsion and bubble phases proportionally to their fractions in the bed [41]. As part of the gas phase is removed from the bed, the general mass balance is adjusted and the new set of equations for the gas phase leads to Eqs. (24) and (25) for the bubble and emulsion phases respectively. Furthermore, since mass transfer resistances (concentration polarization) for H_2 permeation through this type of membranes are expected, in this work it is assumed a reduction of 40% in the extent of H_2 permeation compared to the ideal permeation given by the parameters presented in Table 5. This is done based on previous literature data [26,42], and it is implemented in the model as the mass transfer resistance coefficient β presented in Eq. (22) and that has (in this work) a constant value of 0.6. A more detailed description of the concentration polarization is outside the scope of this work and will be incorporated in the model in the future.

Bubble phase:

$$\frac{\partial}{\partial z}[u_b(f_b + f_w\varepsilon_{mf})C_{i,bw}] = K_{i,be}(f_b + f_w\varepsilon_{mf})(C_{i,ce} - C_{i,bw}) - (f_b + f_w\varepsilon_{mf})\frac{P_{m,Pd}}{t_{m,Pd}}(P_{H2,bw}^n - P_{H2,per}^n) \pm R_{i,bw}f_{bw}(1-\varepsilon_{mf}) \quad (24)$$

Emulsion Phase:

$$\frac{\partial}{\partial z}[u_{g,e}(f_{ce}\varepsilon_{mf})C_{i,ce}] = -K_{i,be}(f_b + f_w\varepsilon_{mf})(C_{i,ce} - C_{i,bw}) - (f_{ce}\varepsilon_{mf})\frac{P_{m,Pd}}{t_{m,Pd}}(P_{H2,ce}^n - P_{H2,per}^n) \pm R_{i,ce}f_{ce}(1-\varepsilon_{mf}) \quad (25)$$

The resulting system of equations is solved using a standard finite difference technique with a first order upwind scheme for the convection terms and Newton-Raphson's method. In total 3000 grid cells are required for grid independent solutions and since the bubble growth is controlled by bubble breakage and the ratio of the bed height over the diameter is relatively high, axial back mixing can be ignored in the model. The boundary and operating conditions and parameters used in

Table 2
General mass balance equations for the solids phase and equations used for the calculation of solids velocities.

Bubble phase: $\frac{\partial}{\partial z}[u_b f_w(1-\varepsilon_{mf})C_{i,w}] = K_{i,we}f_w(1-\varepsilon_{mf})(C_{i,ce} - C_{i,w}) \pm R_{i,w}f_w(1-\varepsilon_{mf})$			(12)
Emulsion phase: $\frac{\partial}{\partial z}[u_{s,e}f_{ce}(1-\varepsilon_{mf})C_{i,ce}] = -K_{i,we}f_w(1-\varepsilon_{mf})(C_{i,ce} - C_{i,w}) \pm R_{i,ce}f_{ce}(1-\varepsilon_{mf})$			(13)
Solid emulsion velocity	$u_{s,e} = \frac{f_w(1-\varepsilon_{mf})u_b + feed/A}{f_{ce}(1-\varepsilon_{mf})}$		(14)
Mass transfer coefficients solid phase	$K_{i,we} = \frac{0.075(u_0-u_{mf})}{u_{mf}d_b} if \frac{u_0}{u_{mf}} \leqslant 3$ $K_{i,we} = \frac{0.15}{d_b} if \frac{u_0}{u_{mf}} > 3$	[38]	(15)

Table 3
Kinetic expressions for the heterogeneous catalyzed reactions proposed by Numaguchi and Kikuchi [39].

Steam methane reforming (16)

$$r_{SMR} = \frac{k_{SMR}\left(P_{CH_4}P_{H_2O} - \frac{P_{H_2}^3 P_{CO}}{K_{p,SMR}}\right)}{P_{H_2O}^{1.596}}\varepsilon_s\rho_{cat}$$

Water gas shift (17)

$$r_{WGS} = \frac{k_{WGS}\left(P_{CO}P_{H_2O} - \frac{P_{H_2}P_{CO_2}}{K_{p,WGS}}\right)}{P_{H_2O}}\varepsilon_s\rho_{cat}$$

With the equilibrium constants

$$K_{p,SMR} = exp(\frac{-2683}{T} + 30.114)$$

$$K_{p,WGS} = exp\left(\frac{4400}{T} - 4.036\right)$$

And the reaction rate constants can be calculated from the Arrhenius equation

$$k = k_0 exp\left(\frac{-E_A}{RT}\right)$$

With the following catalytic reactions parameters:

For SMR: $k_0 = 2.62\cdot10^5 \frac{mol}{bar^{0.404} kg_{cat} s}$ and $E_A = 106.780 \frac{kJ}{mol}$

For WGS: $k_0 = 2.45\cdot10^2 \frac{mol}{bar kg_{cat} s}$ and $E_A = 54.531 \frac{kJ}{mol}$

Table 4
Expressions used for the gas-solid reactions kinetics [30].

$$r_{Ni} = \frac{\varepsilon_{s,p}\rho_s\omega_{act}^0}{b\cdot M_j}\frac{dX_j}{dt} \quad (18)$$

$$\frac{dX_j}{dt} = \frac{\frac{3C_g^n}{b\cdot r_0\cdot C_s}}{(\frac{1}{k}(1-X)^{-\frac{2}{3}} + \frac{r_0}{D}(1-X)^{-\frac{1}{3}} - \frac{r_0}{D})} \quad (19)$$

$$k = k_0 exp\left[-\frac{E_A}{R\cdot T}\right] \quad (20)$$

$$D = D_0 exp\left[-\frac{E_D}{R\cdot T}\right] exp[-k_x X] \quad (21)$$

With the following derived kinetic parameters:

	H_2	CO	O_2
C_s [mol/m^3]	89,960	89,960	151,200
r_o [m]	$3.13\cdot10^{-8}$	$3.13\cdot10^{-8}$	$5.8\cdot10^{-7}$
k_o [m/s]	$9.00\cdot10^{-4}$	$3.5\cdot10^{-3}$	$1.2\cdot10^{-3}$
E_A [kJ/mol]	30	45	7
n	0.6	0.65	0.9
D_0 [m^2/s]	$1.70\cdot10^{-3}$	$7.4\cdot10^6$	1
E_D [kJ/mol]	150	300	0
k_x	5	15	0
b	1	1	2

Table 5
Main parameters used for the description of the membrane permeation in the model.

Fick's law expression $J_{H2} = \beta\frac{P_{m,Pd}}{t_{m,Pd}}(P_{H2,ret}^n - P_{H2,per}^n)$ (22)

Permeability $P_{m,Pd} = P_{m,Pd0}\exp(-\frac{E_{act,Pd}}{RT})$ (23)

With the following parameters

$t_{m,Pd} = 5.0\cdot10^{-6}$	[m]
$P_{m,Pd0} = 4.24\cdot10^{-10}$	[mol/s/m/Pa$^{0.74}$]
$E_A = 5.81$	[kJ/mol]
$n = 0.74$	[–]

the model have been set equal to the conditions tested in the experimental facility, viz. temperatures or inlet gas compositions.

3. Experimental methods

3.1. Description of the setup

A scheme of the lab-scale setup used for the experimental activities is presented in Fig. 4. The fuel reactor (1) is a bubbling fluidized bed of 0.065 m i.d. with a bed height of 0.20 m, and has an empty space of 0.10 m below the porous distributor to preheat the inlet gas. From the freeboard of the bubbling bed, the reduced oxygen carrier particles are transported towards the air reactor. A loop seal (2) is placed in between the two reactors to avoid gas bypass. The air reactor (3) consists of a bubbling bed of 0.05 m i.d. and 0.15 m height connected to a riser reactor (4) of 0.015 m i.d. and 2 m height, where the oxidized carrier particles are accelerated and transported towards a cyclone (5). Oxidized particles are separated in the cyclone and driven to a vessel (6) where particles are collected creating an overpressure through a fixed bed that restricts gas bypass between the reactors. This vessel is connected to a manual gate valve (7) that controls when solids move towards the fuel reactor. The outlet of the gate valve is connected to a 0.008 m o.d. stainless steel tube (8) from where solids fall into the freeboard of the fuel reactor. Therefore, the solids circulation rates are controlled and limited by this tube. To modify the solids circulation rates the diameter of this tube should be changed. Both fuel and air reactors are operated at atmospheric pressure and are placed inside electrical ovens to maintain uniform reaction temperatures, while the remaining parts of the setup (until coolers) are insulated to reduce heat losses.

The oxidized particles falling into the fuel reactor are partially reduced in the freeboard with the unconverted species (CO, CH_4 and H_2) leaving the fuel reactor, which leads to two advantages: partly reduced oxygen carrier (Ni) is fed to the fuel reactor to start the catalytic reactions and the flue gas leaving the fuel reactor consists, ideally, of a mixture of CO_2 and H_2O. The particle size of the oxygen carrier ranges from 150 to 250 μm and its minimum fluidization velocity has been measured at different temperatures with the standard pressure drop method. More detailed information on this oxygen carrier can be found in previous works [30]. Three metallic supported Pd-based membranes (9) have been immersed in the fuel reactor and are connected to a vacuum pump (10) to provide the driving force for gas separation. The support material of these membranes is Hastelloy-X and they are 0.13 m in length and $9.5\cdot10^{-3}$ m in diameter and are similar to other membranes already presented in the literature [24,40], where a Pd selective layer of ~4–5 μm was measured. The permeate flow rate is measured with a mass flow meter (11) connected downstream of the vacuum pump. This allows the measurement of two parameters that indicate the performance of the membrane: (i) the hydrogen recovery factor (HRF) and (ii) the separation factor (SF) and that are defined as in Eqs. (26) and (27) respectively.

Hydrogen recovery factor $HRF = \frac{\varnothing_{H_2,permeated}}{4\varnothing_{CH_4,in}}$ (26)

Separation factor $SF = \frac{\varnothing_{H_2,permeated}}{\varnothing_{H_2,total}}$ (27)

The inlet gas and steam streams are controlled by mass flow controllers and a controlled evaporator mixer (12) respectively supplied by Bronkhorst. N_2 is fed in the loop seal to move the solids from the fuel to the air reactor and avoid mixing of the methane fed to the fuel reactor with air introduced through the bottom distributor to the air reactor. In a real process system, steam should be used in the loop seal since it can be separated afterwards by condensation. Air (undiluted or diluted with N_2) is fed to the air reactor. The outlet composition of the gases is analyzed with an in-line IR analyzer (model Sick GMS815P) (13). To prevent damage of the analyzer, fine particles are removed using solid filters (14) of 40 μm mesh size and the steam is condensed in coolers (15) to avoid that water enters the IR analyzer. Safety valves and gas sensors have also been installed throughout the setup to avoid any kind of pressure increase that might damage the installation and to detect possible gas leaks. Pictures of the experimental facility are provided in Fig. 5.

3.2. Design of experiments

The two reactors are heated up in N_2 at a heating rate of 2 °C/min. The riser, cyclone and vessel are heated up by the solids circulating

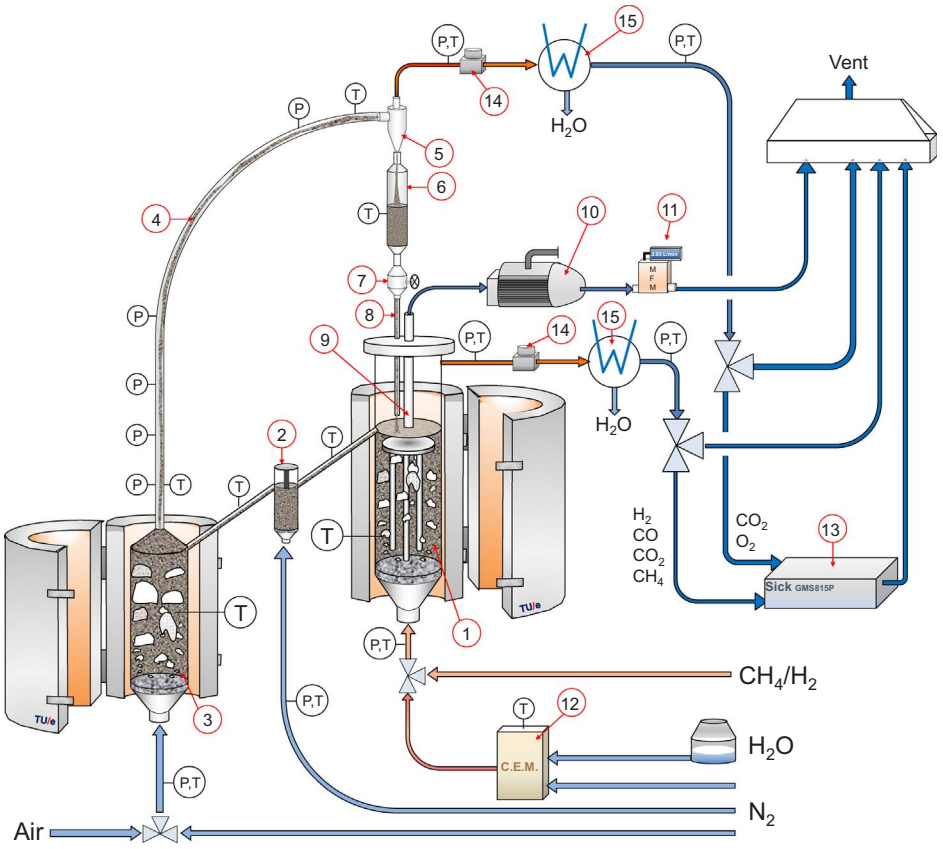

Fig. 4. Detailed scheme of the setup designed in this thesis. 1-fuel reactor; 2-loop seal; 3-air reactor; 4-riser; 5-cyclone; 6-vessel; 7-gate valve; 8-discharge tube; 9-membranes; 10-vacuum pump; 11-mass flow meter; 12-C.E.M.; 13-analyzer; 14-filters; 15-coolers.

between the two reactors. The total inventory is 2.5 kg of oxygen carrier. For the experiments the gate valve is first closed to create a sufficiently long fixed bed in the vessel to completely seal the two reactors. Afterward, the valve is slightly opened and the system adjusts itself without any gas bypass. This fact has been confirmed by feeding CO_2 traces in one of the reactors and analyzing the outlet composition of the exhaust of the other reactor. The performance of the membranes has been checked on a daily basis by measuring the permeability and ideal perm-selectivity always at the same temperature (480 °C). In total, the setup has been operated for more than 100 h of operation (including inert gas tests by feeding only N_2 to the two reactors). The temperature oscillations at different positions throughout the setup and pressure fluctuations in the riser are indicators of the presence of solids circulation.

Different experimental conditions have been selected in order to demonstrate that pure H_2 can be produced with the MA-CLR concept. In particular, experiments have been done first with a CLR configuration, thus without membranes. Subsequently, the immersed membranes in the fuel reactor are opened and the vacuum pump is connected to extract H_2 selectively, thus operating the reactor in the Membrane-Assisted Chemical Looping Reforming configuration. For all the cases a methane concentration of 20% (vol.) is selected, while the steam to carbon (S/C) ratio and the amount of oxygen fed to the air reactor (thus the overall O/C ratio) have been varied to gain more knowledge on the behavior of this concept. N_2 is used as carrier gas for the quantification of the results, and the split fraction of the N_2 in the loop seal (N_2 going towards fuel and air reactors) is quantified by solving the carbon balance. Carbon deposition (if any) is also quantified by measuring the CO_2 concentration in the air reactor flue gas line. A list of the experiments carried out is presented in Table 6.

4. Results and discussion

4.1. Experimental demonstration

For all the results presented in this section, first the experiments have been carried out with the permeate side closed, thus in a CLR configuration. Steady state is reached almost immediately and continuous operation is kept for at least 20 min. After this period the membranes are opened and the vacuum pump is turned on. Immediately, a change in the concentration profiles in the fuel reactor is observed because of the displacement of the equilibrium. Simultaneously, the amount of H_2 permeating through the membranes is measured to quantify the hydrogen recovery factor (HRF) and separation factor (SF). A complete screening of the reaction in the CLR and the MA-CLR configurations is presented in Fig. 6, where the outlet composition of the fuel reactor and the temperatures throughout the setup are presented. The oscillations observed in the temperatures, especially for the air reactor, are caused by the continuous movement of the oxygen carrier through the setup. When relatively cold particles enter the air reactor, the temperature inside sharply decreases. On the other hand, when the solids flux is temporarily reduced, the temperature increases rapidly because of the oxidation reactions occurring inside the reactor. During the experimental screening, some attrition of the solid material was observed since around 0.5 g of powder was collected per day from the filters. This small amount of powder slightly increased the pressure drop in the filters, although no influence on the system was evidenced. Every day the filters were cleaned to assess reproducibility of the results.

The results obtained from the experiments in Table 6 have been compared with a thermodynamic analysis done in Aspen Plus for the fuel reactor in the CLR configuration. Since oxygen is part of the process and enters the fuel reactor via its freeboard, thermodynamic calculations are carried out as two consecutive isothermal Gibbs reactors. In

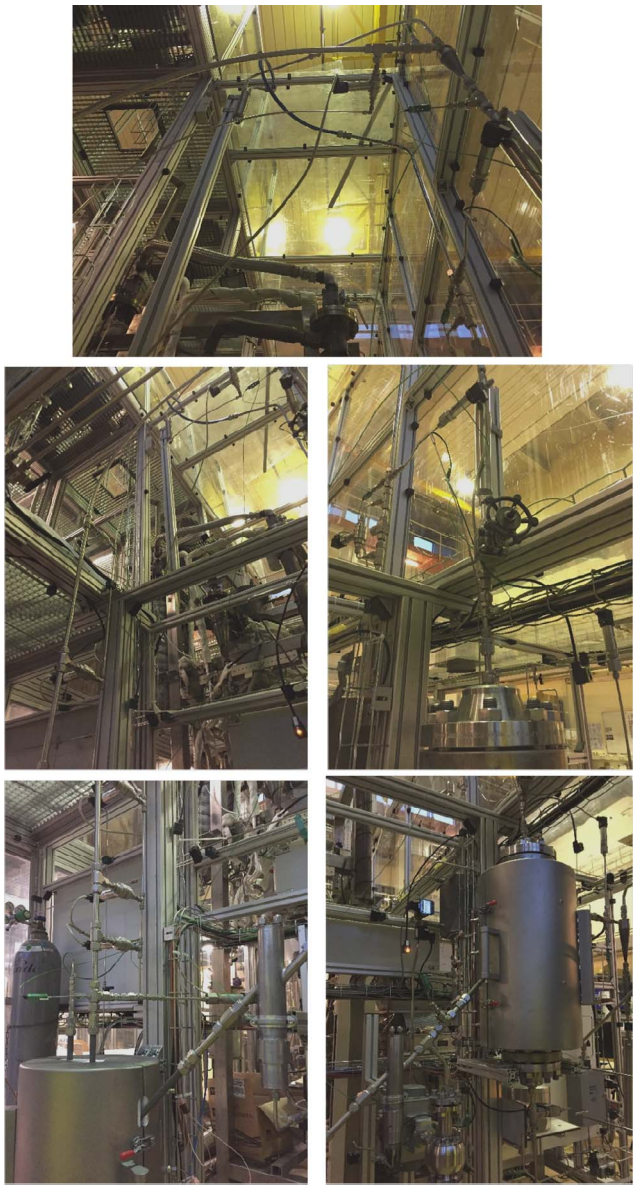

Fig. 5. Pictures of the installation used in this work. Bottom left: air reactor inside the electrical oven and loop seal. Left: riser with pressure sensors; top: cyclone; right: vessel and gate valve; bottom right: fuel reactor inside the oven and loop seal.

the first Gibbs reactor, the equilibrium of the feed gas in the fuel reactor is calculated. Subsequently, the flue gas is mixed in a second Gibbs reactor (at the same temperature) with the calculated amount of oxygen introduced into the fuel reactor. The amount of oxygen participating in the reaction in the fuel reactor is calculated based on the O_2 fed to the air reactor and the amount of O_2 measured in the analyzer at the outlet of the air reactor line. In particular, all the oxygen is used for the oxidation of the oxygen carrier when feeding diluted air (5% of oxygen). Contrary, when undiluted air is fed to the air reactor, oxygen is detected in the exit gas stream and the oxygen concentration ranges from 4 to 8% (vol.) depending on the air reactor temperature. Therefore, it is a

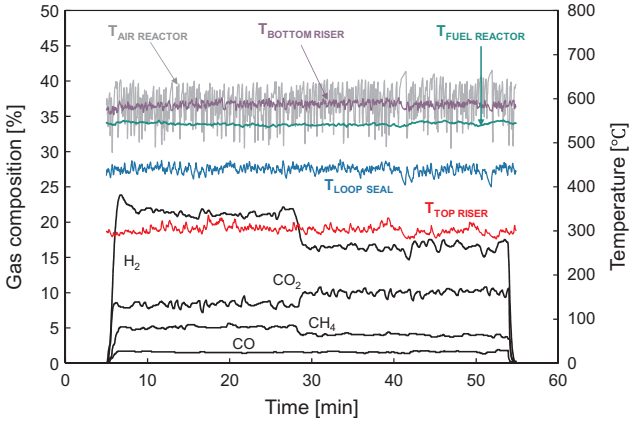

Fig. 6. Gas concentration profiles at the outlet of the fuel reactor and temperature distribution throughout the lab-scale reactor at the following conditions: Temperature fuel reactor = 550 °C; Temperature air reactor = 600 °C; Undiluted air fed to the air reactor; S/C ratio = 2.

measurement of the overall oxygen to carbon (O/C) ratio inside the fuel reactor, which is in its turn used in the second Gibbs reactor. For all the cases CO_2 was not detected (< 0.2%vol.) in the air reactor exhaust stream, thus carbon deposition can be neglected at steady state conditions.

The methane conversion is presented in Fig. 7 (for a S/C ratio of 3) and Fig. 8 (S/C ratio of 2) as function of the temperature and the amount of oxygen fed to the air reactor. At a first glance to the results, it is found that the MA-CLR configuration clearly outperforms the CLR configuration for all the conditions. This is expected since the thermodynamic equilibrium is displaced by selective separation of H_2. Furthermore, it is also observed that in all the cases, the methane conversion increases as a function of the temperature (the reaction equilibrium is favored at higher temperatures) and also as a function of the amount of oxygen fed to the air reactor. This fact is related to the partial oxidations occurring inside the fuel reactor with the oxygen transferred from the air reactor. However, the fact that partial oxidations are occurring inside the fuel reactor also leads to a decrease in the selectivity of the process towards H_2 production since gas solid reactions between the NiO and H_2 and CO are occurring inside the bed. Actually, it is confirmed experimentally that in absence of oxygen in the feed to the air reactor, all the converted CH_4 goes to H_2 and CO as for the SMR reaction. However, for the cases where 5 and 21 vol% of oxygen is fed to the air reactor, the selectivity towards hydrogen decreases to a value around 80 and 60% respectively, as measured experimentally. This indicates that part of the H_2 produced during reforming is reacting with the oxygen contained in the oxygen carrier.

When decreasing the steam to carbon ratio similar conclusions can be obtained, with the only difference that slightly lower conversions are obtained. For both steam to carbon ratios similar trends are observed regarding the influence of temperature and amount of O_2 in the feed to the air reactor. At low temperatures (< 550 °C) it is observed that the calculated equilibrium is not reached in the CLR configuration and it becomes closer at slightly higher temperatures. Only at temperatures around 600 °C in the fuel reactor the thermodynamic equilibrium is fully achieved with the CLR configuration, whereas the thermodynamic limitations are overcome with the MA-CLR configuration. This can be explained by the fact that the kinetics of gas-solid reactions are largely

Table 6
Experimental conditions investigated in order to demonstrate the MA-CLR concept.

Configuration	T_{FR} [°C]	T_{AR} [°C]	F_{CH4} [L/min]	$u_0/u_{mf,FR}$	$u_0/u_{mf,AR}$	$O_{2,AR}$ [%vol.]	S/C ratio
CLR	450–600	500–650	0.75–1	2–3	3–5	0–5–21	2–3
MA-CLR	450–600	500–650	0.75–1	2–3	3–5	0–5–21	2–3

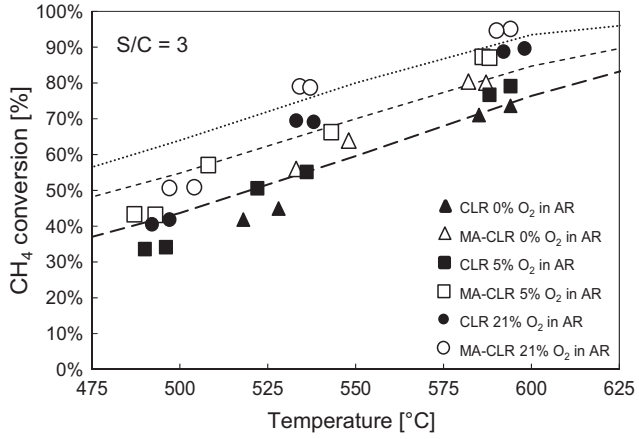

Fig. 7. Methane conversion as a function of temperature and oxygen content in the feed to the air reactor for the CLR and MA-CLR configurations and a steam to carbon ratio of 3. The solid lines represent the equilibrium for 0, 5 and 21% O_2 in the air reactor based on the calculated oxygen to carbon ratio in the fuel reactor.

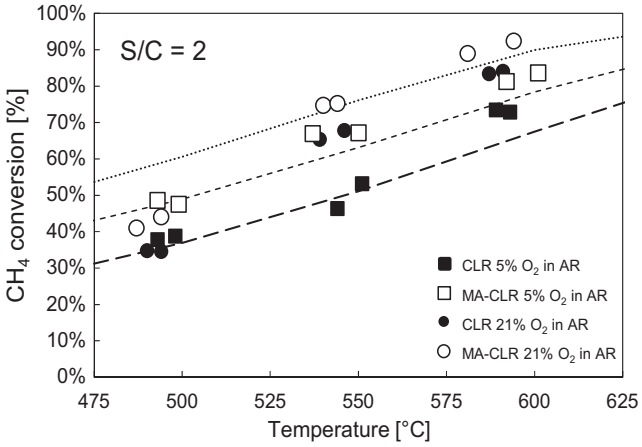

Fig. 8. Methane conversion as a function of temperature and oxygen content in the feed to the air reactor for the CLR and MA-CLR configurations and a steam to carbon ratio of 2. The solid lines represent the equilibrium for 0, 5 and 21% O_2 in the air reactor based on the calculated oxygen to carbon ratio in the fuel reactor.

influenced by temperature [30]. Therefore, at lower temperatures a lower amount of reduced Ni particles are available in the fuel reactor with a corresponding decrease in the extent of catalytic reactions. On the other hand, when increasing the temperature, a higher extent of gas-solid reactions occur and thus more reduced Ni is available in the bed for the reforming reaction, hence the calculated equilibrium can be achieved.

Since H_2 permeation is monitored during the experiments, the hydrogen recovery factor (HRF) and separation factor (SF) can be calculated for all the experiments carried out under the MA-CLR configuration, and the results are presented in Fig. 9.

The hydrogen recovery factor follows an increasing trend as a function of the temperature and steam to carbon ratio. This is related to the higher conversions achieved at these conditions, which in its turn lead to higher amounts of H_2 in the fuel reactor with a corresponding increase in the H_2 partial pressure, and thus the driving force for selective H_2 separation. In particular, for a higher S/C ratio, the effect of a higher CH_4 conversion is more important than the increased gas dilution, which then results in an increase in the H_2 permeation rate through the membranes. In the experiments carried out feeding undiluted air to the air reactor, a decrease in the HRF compared to the other experiments at similar temperatures and S/C ratios is observed, which is attributed to the increase in the extent of the gas-solid reactions between the NiO and H_2 in the fuel reactor. In general, a maximum HRF of 30% is achieved due to the limited fuel reactor operating pressure.

On the other hand, the separation factor follows a slightly decreasing trend as a function of temperature and it is less dependent on the S/C ratio and the amount of oxygen fed to the air reactor. The fact that all the values are rather similar is associated to the fact that the SF depends on the minimum H_2 partial pressure difference between the retentate and permeate side, which is very relevant in this case since the setup is operated at atmospheric conditions. In general, the higher the temperature, the higher the amount of H_2 permeating through the membranes, as can be concluded from the HRF plot. However, when H_2 is separated through the membranes, its partial pressure decreases inside the bed to values where the driving force is small and almost no more hydrogen can be extracted, which is a common factor for all the cases, as concluded from the SF plot. During the whole set of experiments the ideal perm-selectivity of the membranes has been measured at a fixed temperature of 480 °C. At the beginning of the experiments the ideal perm-selectivity measured was 5400, thus indicating high H_2 purities in the permeate stream. This value was rather constant and after the whole set of experiments the measured ideal perm-selectivity was only slightly lower (4890). Therefore, good stability of the membranes (and their sealing) has been confirmed.

From the experimental results, and more precisely based on the SFs measured, it is observed that the system is limited by H_2 separation through the membranes since the SF reaches a maximum (and constant) value of about 40–45%. In order to increase the recoveries and concomitant fuel conversion, an increase in the operating pressure and/or on the membrane surface area is required. While the setup was not designed for installing more membranes, an increase in the operating pressure in these type of reactors currently represents a technological challenge.

Since the solids circulation rates are fixed by the 8 mm o.d. tube connected from the gate valve to the fuel reactor, the influence of solids circulation rates on the performance of the process has not been investigated in this work. However, based on pressure drop measurements along the riser (using the method described in Medrano et al. [43]), an average value of 10 g/s has been measured for all the conditions. This is expected since they are fixed with the current configuration of the chemical looping facility. The solids circulation rates and the influence on the reactor performance will be investigated in a future work after some modification of the setup.

4.2. Model validation

The model developed in this work has been validated with the

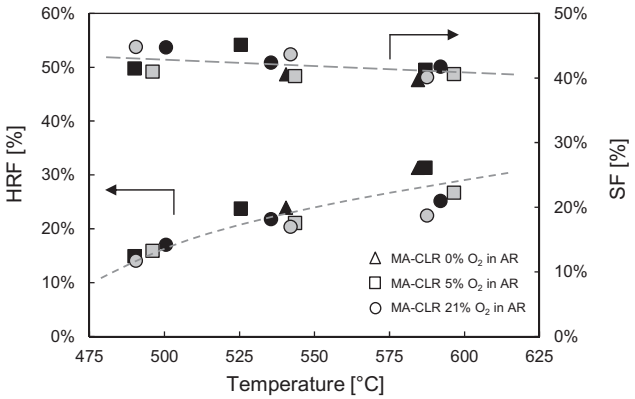

Fig. 9. Hydrogen recovery factor (HRF) and separation factor (SF) measured experimentally in the MA-CLR configuration for different operating conditions. Black markers represent experiments with a steam to carbon ration of 3, while gray markers indicate the experiments carried out with a steam to carbon ratio of 2.

experimental results presented in the previous section in terms of methane conversion, HRF and SF. Thanks to the model it is possible to predict the gas concentration profiles inside the reactors as well as the solids phase compositions in both reactors as a function of the different operating conditions. Typical profiles are presented in Fig. 10 and Fig. 11, where the solids phase compositions and gas concentration profiles along both air and fuel reactors, in the bubble and emulsion phases are presented. These results are for a fuel and air reactor temperatures of around 600 °C, a steam to carbon ratio of 3 in the fuel reactor and 5% of O_2 fed to the air reactor (diluted air in N_2).

Since a small amount of oxygen is fed into the air reactor (5% vol.), not all the Ni is oxidized to NiO in the air reactor. This leads to a common fraction of around 60/40 Ni/NiO at steady state conditions (the Ni loading onto the support material is 20%). If pure air is to be used in the air reactor, then almost all the active solid material is NiO (> 95% of Ni → NiO conversion). On the other hand, it is observed in the fuel reactor that almost the entire solid phase is present as Ni. This is mostly associated to the fast kinetics for NiO reduction at these temperatures with CO and H_2 and also to the fact that the amount of O_2 in the oxygen carrier is sub-stoichiometric. This behavior corresponds to the expected one in the real process, where the overall amount of O_2 to the fuel reactor is fixed to achieve auto-thermal operation and the solid phase should be working as a catalyst for the reforming reactions in the fuel reactor. At lower temperatures a higher concentration of NiO in the fuel reactor is observed due to diffusion limitations for NiO reduction. In fact, a fraction of around 10% of NiO is observed in the fuel reactor (65% in the air reactor) for a similar case as before when operating the two reactors at around 500 °C.

Regarding the gas concentration profiles along the fuel reactor (Fig. 11), it is observed that the system goes fast to the equilibrium at the bottom of the reactor. As soon as the permeation starts at an axial position of 0.04 m (and until 0.17 m) this equilibrium is shifted because of the selective removal of H_2 through the three membranes, as can be discerned from the figure. By comparing the concentration profiles in both phases, some bubble to emulsion mass transfer limitations can be observed, although not enough to largely influence the results. This is explained by the relative small bubble (and wake) fraction in the bed compared to the emulsion phase (Fig. 12 left). It should also be remarked that the reforming reaction leads to molar expansion in the bed, thus increasing the superficial gas velocity with a corresponding increase in the bubble fraction in the bed. However, since H_2 is separated from the bed through the membranes, this implies an important decrease in the superficial gas velocity (Fig. 12 right) with a corresponding overall decrease in the bubble fraction. Moreover, it is also assumed that a small amount of particles is present inside the bubbles, which means that reaction is also occurring in the bubble phase. Overall, it leads to a relatively small influence of the bubble to emulsion mass transfer limitations.

For the modeling case presented in these figures, the measured methane conversion is 86%, while the total amount of H_2 permeated through the membrane is 0.048 mol/h (1.1 L_{H2}/min), resulting in a HRF of 29.3%. This is in a good agreement with data obtained experimentally at the same operating conditions as presented in Table 7.

The results of the validation are presented in Table 7 for different steam to carbon ratios, temperatures and amount of oxygen in the feed to the air reactor. In general, the model can describe quite well the experimental results for all the conditions, although some deviations are observed. In particular, deviations between ± 10–20% are highlighted in light gray, while deviations above ± 20% are highlighted in dark gray. The average deviation in the model predictions compared with the experimental data is below 10%.

Giving a closer look to the results presented in Table 7, it is observed that relatively large deviations are only measured at low temperatures (around 500 °C). This could be explained, especially for the case of 0% O_2 fed to the air reactor, by a larger amount of NiO particles inside the fuel reactor in the experiments. In a previous work it was observed that full NiO reduction with H_2 or CO is not occurring at temperatures below 600 °C [30]. Since the experiments are carried out at relatively low temperatures (and the solid phase is not reduced in between experiments at higher temperatures to avoid damage of the membranes), there is an accumulation of unconverted NiO inside the reactor that is not accounted for in the model. This implies a lower amount of reduced Ni particles for the catalytic reforming reaction in the fuel reactor, which in its turn leads to a lower extent of methane conversion. At 500 °C, only in the experiments with a S/C ratio of 2 there is no important discrepancy between the model and experimental results. This is explained by the fact that these experiments were carried out after the experiments at 600 °C, where the NiO was reduced to Ni. On the other hand, for the experiments carried out at higher temperatures, it is observed that the model can predict the experimental results adequately.

The modeling results in terms of HRF and SF also show a good agreement with experimental data and they both follow the same trends as measured experimentally. If concentration polarization were not accounted for in the model, the extent of H_2 permeation would be largely increased resulting in a higher methane conversion, HRF and SF.

In this work it can be concluded that the phenomenological model has been validated and that it can adequately predict the performance of the MA-CLR. However, the validation has only been done on the basis of the outlet compositions from the reactor exhaust streams, but not on the gas concentration or solids phase profiles along the reactors. To do so, several adjustments should be done to the experimental facility in order to take measurements at intermediate positions in the bed and to take samples of the solid material at different axial positions. Furthermore, the installation of solids sampling points at the inlet/outlet of the reactors would allow the determination of the reduction state of the oxygen carrier. Therefore, still more research is needed in order to further validate the model for the MA-CLR concept.

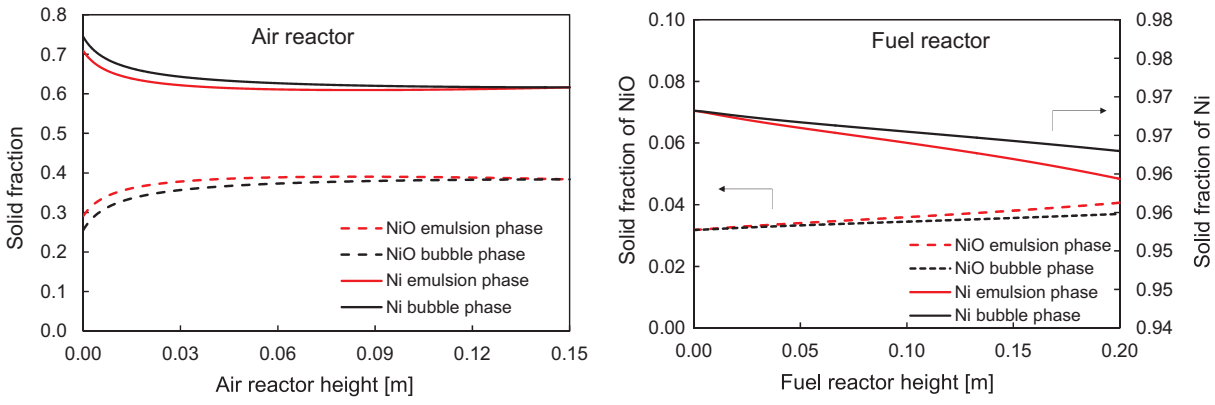

Fig. 10. Ni/NiO profiles in the fuel and air reactors for the bubble and emulsion phases for a case of 588 °C in the fuel reactor, S/C 3 and 5% O_2 in the air reactor operated at 596 °C.

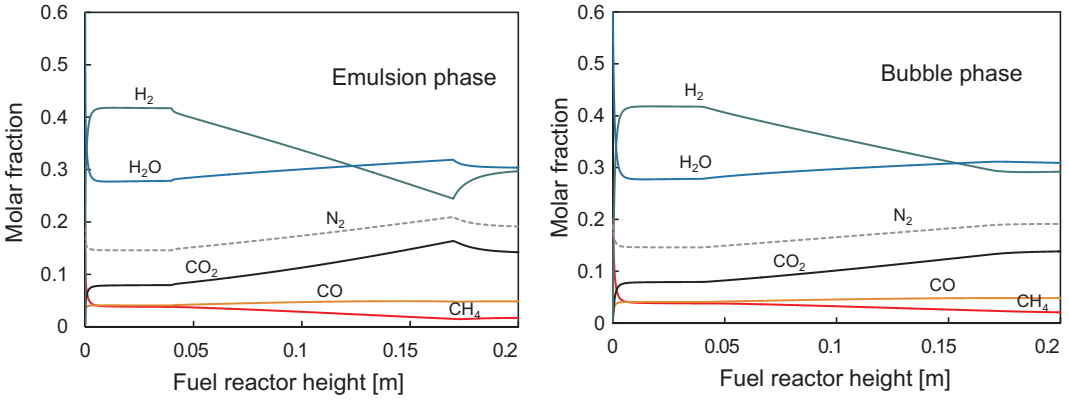

Fig. 11. Gas concentration profiles in the fuel reactor for the bubble and emulsion phases for a case of 588 °C in the fuel reactor, S/C 3 and 5% O_2 in the air reactor operated at 596 °C.

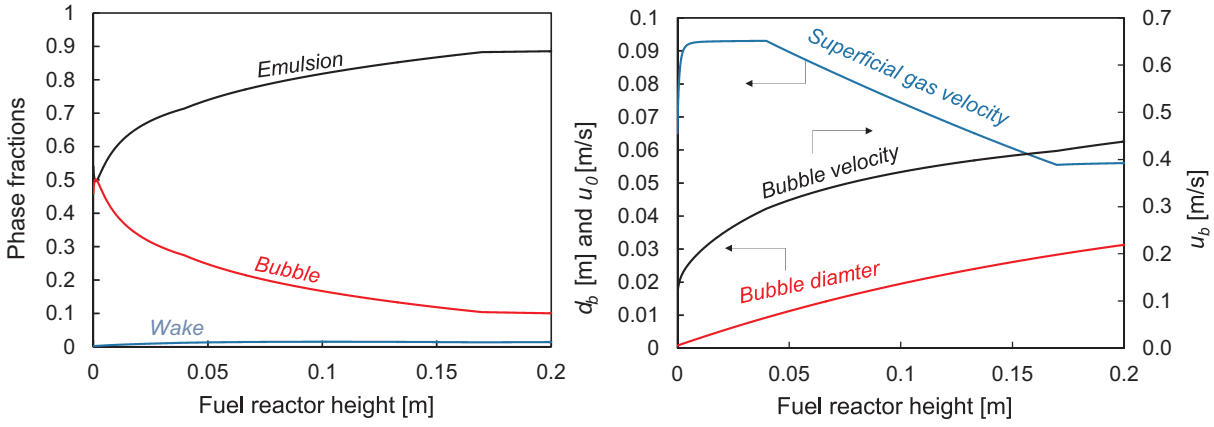

Fig. 12. Profiles of phase fractions (left) and bubble properties and superficial gas velocity (right) as a function of the fuel reactor height for a modeling case of 588 °C in the fuel reactor, S/C 3 and 5% O_2 in the air reactor operated at 596 °C.

Table 7
Comparison between experimental data and modeling results in terms of methane conversion, hydrogen recovery factor (HRF) and separation factor (SF). Values highlighted in light gray represent deviations within 10–20% and values highlighted in dark gray indicate deviations above 20%.

		Chemical Looping Reforming			Membrane-Assisted Chemical Looping Reforming (MA-CLR)						
Conditions		Methane conversion			Methane conversion			H_2 Recovery Factor		Separation Factor	
S/C ratio	$O_{2\ AR}$ [%]	T_{FR} [°C]	Exp. [%]	Model [%]	T_{FR} [°C]	Exp. [%]	Model [%]	Exp. [%]	Model [%]	Exp. [%]	Model [%]
3	0	528	44.9	55.1	533	55.9	65.8	23.4	24.0	41.4	39.9
		594	73.6	77.9	582	80.3	82.9	31.2	28.9	39.6	40.0
3	5	496	34.1	42.2	493	43.2	52.2	14.8	19.3	41.7	40.2
		536	55.1	60.3	543	66.3	71.1	27.0	24.8	46.4	40.2
		594	79.1	79.7	588	87.0	86.0	31.6	29.3	41.5	40.6
2	5	498	38.8	38.2	499	47.6	48.3	16.0	17.9	40.7	40.9
		551	53.2	57.9	550	67.1	66.2	19.9	23.2	38.7	41.4
		593	72.9	73.1	601	83.6	83.1	27.0	27.5	40.8	41.8
Average deviation [%]				8.73			6.70		10.8		4.21

Nevertheless, the model can be used for the design of scaled-up reactors as well as quantification of the number of membranes needed to achieve a target recovery (target H_2 production), which already represents an important achievement for the further development of this reactor concept.

5. Conclusions

In this work the MA-CLR concept has been demonstrated at lab scale conditions. In this concept pure H_2 has been separated from the fuel reactor through palladium-based membranes while the Ni-based oxygen carrier was circulating between the air and fuel reactors, which in case of negligible heat losses would lead to autothermal operation. Experiments have been carried out at different conditions and the best results, in terms of HRF, have been found at high temperatures and a low amount of oxygen fed to the air reactor (5%), which gives an overall oxygen to carbon ratio (O/C) of 0.25, commonly recommended for autothermal operation in CLR units. In the case the process is carried out in absence of O_2 in the air reactor, the concept would not work at autothermal conditions. When undiluted air is used in the air reactor, the selectivity towards H_2 largely decreases (to around 60%) and it also results in a lower HRF since the O/C ratio is increased.

Together with the experimental demonstration, a phenomenological model has been developed and validated, which also accounts for bed-to-membrane mass transfer resistances. Overall, a discrepancy of only 7% is achieved for the methane conversion compared with experimental data, while the deviations for the HRF and SF factors are 11% and 4% respectively, thus resulting in a quite acceptable accuracy of the model. Thus, this model can be used to predict the behavior of the MA-CLR at different operating conditions and scales, which in its turn can help optimizing and designing scaled-up experimental versions of this reactor concept.

Acknowledgements

NWO/STW is acknowledged for the financial support through the VIDI project number 12365. Special thanks also to J.P. Kors for the constructions and maintenance of the experimental setup and A. Battistella for the assistance with the model.

References

[1] IPCC, Climate Change 2014: Synthesis Report. Contribution of Working Groups I, II and III to the Fifth Assessment Report of the Intergovernmental Panel on Climate Change; 2014.
[2] IPCC. IPCC Special Report on Carbon Dioxide Capture and Storage. Cambridge (UK): Cambridge University Press; 2005.
[3] IEA, Energy technology perspectives: scenarios and strategies to 2050, Paris, France: OECD/IEA; 2010.
[4] Kenarsari SD, Yang D, Jiang G, Zhang S, Wang J, Russell AG, et al. Review of recent advances in carbon dioxide separation and capture. RSC Adv 2013;3:22739–73.
[5] Spallina V, Pandolfo D, Battistella A, Romano MC, van Sint Annaland M, Gallucci F. Techno-economic assessment of membrane assisted fluidized bed reactors for pure H_2 production with CO_2 capture. Energy Convers Manage 2016;120:257–73.
[6] Ball M, Wietschel M. The future of hydrogen – opportunities and challenges. Int J Hydrogen Energy 2009;34:615–27.
[7] Lewis W, Gulliland E. Production of pure carbon dioxide. US2665971; 1954.
[8] Richter HJ, Knoche KF. Reversibility of combustion processes. ACS Symp. Ser. 1983:71–85.
[9] Ishida M, Zheng D, Akehata T. Evaluation of a chemical-looping-combustion power-generation system by graphic exergy analysis. Energy 1987;12:147–54.
[10] Ishida M, Jin H. A new advanced power-generation system using chemical-looping combustion. Energy 1994;19:415–22.
[11] Adanez J, Abad A, Garcia-Labiano F, Gayan P, de Diego LF. Progress in chemical-looping combustion and reforming technologies. Prog. Energy Combust Sci 2012;38:215–82.
[12] Rydén M, Lyngfelt A, Mattisson T. Synthesis gas generation by chemical-looping reforming in a continuously operating laboratory reactor. Fuel 2006;85:1631–41.
[13] Hossain MM, de Lasa HI. Chemical-looping combustion (CLC) for inherent CO_2 separations—a review. Chem Eng Sci 2008;63:4433–51.
[14] Lyngfelt A. Chemical-looping combustion of solid fuels – Status of development. Appl Energy. 2014;113:1869–73.
[15] Tang M, Xu L, Fan M. Progress in oxygen carrier development of methane-based chemical-looping reforming: a review. Appl Energy 2015;151:143–56.
[16] Forero CR, Gayán P, de Diego LF, Abad a, García-Labiano F, Adánez J. Syngas combustion in a 500 Wth chemical-looping combustion system using an impregnated Cu-based oxygen carrier. Fuel Process Technol 2009;90:1471–9.
[17] Pröll T, Bolhàr-Nordenkampf J, Kolbitsch P, Hofbauer H. Syngas and a separate nitrogen/argon stream via chemical looping reforming – a 140kW pilot plant study. Fuel 2010;89:1249–56.
[18] Sridhar D, Tong A, Kim H, Zeng L, Li F, Fan L. Syngas chemical looping process: design and construction of a 25 kWth Subpilot Unit. Energy Fuels 2012.
[19] Sit S, Reed A, Hohenwarter U, Horn V, Marx K, Proell T. Cenovus 10 MW CLC field pilot. Energy Proc 2013;37:671–6.
[20] Dunn S. Hydrogen futures: toward a sustainable energy system. Int J Hydrogen Energy 2002;27:235–64.
[21] McDowall W, Eames M. Forecasts, scenarios, visions, backcasts and roadmaps to the hydrogen economy: a review of the hydrogen futures literature. Energy Policy 2006;34:1236–50.
[22] Gallucci F, Fernandez E, Corengia P, van Sint Annaland M. Recent advances on membranes and membrane reactors for hydrogen production. Chem Eng Sci 2013;92:40–66.
[23] Gallucci F, Medrano JA, Fernandez E, Melendez J, van Sint Annaland M. Advances on high temperature pd-based membranes and membrane reactors for hydrogen purification and production graphical abstract keywords. J Membr Sci Res 2017;3:142–56.
[24] Medrano JA, Fernandez E, Melendez J, Parco M, Pacheco-Tanaka DA, van Sint Annaland M, et al. Pd-based metallic supported membranes: High-temperature stability and fluidized bed reactor testing. Int J Hydrogen Energy 2016;41:8706–18.
[25] Medrano JA, Julian I, Garcia-Garcia FR, Li K, Herguido J, Menendez M. Two-zone fluidized bed reactor (TZFBR) with palladium membrane for catalytic propane dehydrogenation: Experimental performance assessment. Ind Eng Chem Res 2013;52:3723–31.
[26] Caravella A, Scura F, Barbieri G, Drioli E. Inhibition by CO and polarization in Pd-based membranes: a novel permeation reduction coefficient. J Phys Chem B 2010;114:12264–76.
[27] Gallucci F, van Sint Annaland M, Kuipers JAM. Autothermal reforming of methane with integrated CO_2 capture in a novel fluidized bed membrane reactor. Part 1: experimental demonstration. Top Catal 2008;51:133–45. http://dx.doi.org/10.1007/s11244-008-9126-8.
[28] Gallucci F, van Sint Annaland M, Kuipers JAM. Autothermal reforming of methane with integrated CO_2 capture in a novel fluidized bed membrane reactor. Part 2 comparison of reactor configurations. Top Catal 2008;51:146–57.
[29] Medrano JA, Spallina V, van Sint Annaland M, Gallucci F. Thermodynamic analysis of a membrane-assisted chemical looping reforming reactor concept for combined H_2 production and CO_2 capture. Int J Hydrogen Energy. 2014;39:4725–38.
[30] Medrano JA, Hamers HP, Williams G, van Sint Annaland M, Gallucci F. NiO/$CaAl_2O_4$ as active oxygen carrier for low temperature chemical looping applications. Appl Energy 2015;158:86–96.
[31] Iliuta I, Tahoces R, Patience GS, Rifflart S, Luck F. Chemical-looping combustion process: kinetics and mathematical modeling. AIChE J 2010;56:1063–79.
[32] Kunii D, Levenspiel O. Fluidization engineering. second ed; 1991.
[33] Medrano JA, Tasdemir M, Gallucci F, van Sint Annaland M. On the internal solids circulation rates in freely-bubbling gas-solid fluidized beds. Chem Eng Sci 2017;172:395–406.
[34] Lippens BC, Mulder J. Prediction of the minimum fluidization velocity. Powder Technol. 1993;75:67–78.
[35] Broadhurst TE, Becker HA. Onset of fluidization and slugging in beds of uniform particles. AIChE J 1975;21:238–47.
[36] Mori S, Wen CY. Estimation of bubble diameter in gaseous fluidized beds. AIChE J 1975;21:109–15.
[37] Medrano JA, Gallucci F, Boccia F, Alfano N, van Sint Annaland M. Determination of the bubble-to-emulsion phase mass transfer coefficient in gas-solid fluidized beds using a non-invasive infra-red technique. Chem Eng J 2017;325:404–14.
[38] Gascon J, Tellez C, Herguido J, Jakobsen HA, Menendez M. Modeling of Fluidized bed reactors with two reaction zones. AIChE J 2006;52:3911–23.
[39] Numaguchi T, Kikuchi T. Intrinsic kinetics and design simulation in a complex reaction network: steam-methane reforming. Chem Eng Sci 1988;43:2295–301.
[40] Fernandez E, Medrano JA, Melendez J, Parco M, Viviente JL, van Sint Annaland M, Pacheco Tanaka DA. Preparation and characterization of metallic supported thin Pd–Ag membranes for hydrogen separation. Chem Eng J 2016;305:182–90.
[41] Deshmukh SARK, Laverman JA, Cents AHG, van Sint Annaland M, Kuipers JAM. Development of a membrane-assisted fluidized bed reactor. 1. Gas phase back-mixing and bubble-to-emulsion phase mass transfer using tracer injection and ultrasound experiments. Ind Eng Chem Res 2005;44:5955–65.
[42] Caravella A, Barbieri G, Drioli E. Concentration polarization analysis in self-supported Pd-based membranes. Sep Purif Technol 2009;66:613–24.
[43] Medrano JA, Nordio M, Manzolini G, van Sint Annaland M, Gallucci F. On the measurement of solids circulation rates in interconnected fluidized beds: Comparison of different experimental techniques. Powder Technol 2016;302:81–9.